Synthesis, Structure, and Reactions of Poly(ethylene oxide)/V_2O_5 Intercalative Nanocomposites

Y.-J. Liu,† J. L. Schindler,‡ D. C. DeGroot,‡ C. R. Kannewurf,‡ W. Hirpo,† and M. G. Kanatzidis*,†,§

Department of Chemistry and the Center for Fundamental Materials Research, Michigan State University, East Lansing, Michigan 48824, and Department of Electrical Engineering and Computer Science, Northwestern University, Evanston, Illinois 60208

Received August 7, 1995. Revised Manuscript Received November 28, 1995⊗

The intercalation of poly(ethylene oxide) (PEO) in layered V_2O_5 xerogel and the structural and physicochemical characterization of the products is reported. The synthesis of PEO/V_2O_5 nanocomposites is achieved by simply mixing aqueous solutions of PEO with aqueous V_2O_5 gels followed by slow water evaporation. Several different phases of PEO/V_2O_5 composites can be obtained by varying the component ratios. The interlayer distance of $(PEO)_xV_2O_5{\cdot}nH_2O$ varies from 13.2 Å, at $x = 0.5$, to 16.8 Å at $x = 1.0$, to 17.6 Å at $1 < x < 3$, and to 18.3 Å at $x \geq 3$. One-dimensional electron density calculations based on X-ray diffraction data (perpendicular to layers) show that the composites contain a monolayer of PEO molecules when $x < 1$ and a bilayer when $x \geq 1$. The data suggest that the PEO chains are arranged side-by-side in a fully extended conformation between the layers forming corrugated mono- or bilayers. The $(PEO)_xV_2O_5{\cdot}nH_2O$ intercalation compounds are water swellable and light-sensitive. UV irradiation causes dramatic changes in the electronic structure of V_2O_5 and results in enhanced electrical conductivity and decreased solubility. The conductivity of the irradiated products decreases as the PEO content increases. The optical absorption spectra, electrical conductivity, thermoelectric power, magnetic susceptibility, and electron paramagnetic resonance spectra of the irradiated products are self-consistent and suggest an increased V^{4+} concentration in the layers and n-type charge transport. Lithium ion redox intercalation was performed on the PEO/V_2O_5 composites by reaction with LiI. Variable-temperature ^{7}Li solid-state NMR studies of the Li/PEO/V_2O_5 materials are reported.

Introduction

In recent years, the synthesis of polymer/inorganic nanocomposites has received considerable attention.[1−3] These materials, in principle, can possess electrical, optical, and mechanical properties which may not be achieved with each component separately.[4] V_2O_5 xerogel is a very reactive layered host material[5] which can be intercalated by cation-exchange, acid−base chemistry, or redox reactions. In the past several years, we have reported that monomers such as aniline, pyrrole, and bithiophene can be oxidatively polymerized and intercalated into the intralamellar space of the host.[3,6] Recently, we reported, in preliminary form, the encapsulation of several water-soluble polymers such as poly(vinylpyrrolidone) (PVP), poly(propylene glycol) (PPG), and methylcellulose in V_2O_5 xerogel.[7] PEO has the simplest structure of water-soluble polymers. Its salt complexes have shown to be solid electrolytes and have attracted considerable research attention because they are promising for applications in solid-state batteries and electrochromic devices.[8] Systematic studies of ionic conductivity versus composition and temperature for

† Michigan State University.
‡ Northwestern University.
§ Camille and Henry Dreyfus Teacher Scholar 1993−95.
⊗ Abstract published in *Advance ACS Abstracts,* January 15, 1996.

(1) (a) Ozin, G. A. *Adv. Mater.* **1992**, *4*, 612−649 and references therein. (b) Alcock, H. R. *Science*, **1992**, *255*, 1106 and references therein. (c) Sanchez, C.; Ribot, F. *New J. Chem.* **1994**, *18*, 1007−1047. (d) O'Hare, D. *New J. Chem.* **1994**, *18*, 989−998. (e) Ruiz-Hitzky, E. *Adv. Mater.* **1993**, *5*, 334−340. (f) Ruiz-Hitzky, E.; Aranda, P.; Casal, B.; Galvan, J. *Adv. Mater.* **1995**, *7*, 180−184.

(2) (a) Day, P.; Ledsham, R. D. *Mol. Cryst. Liq. Cryst.* **1982**, *86*, 163−174. (b) Tieke, B. *Mol. Cryst. Liq. Cryst.* **1983**, *93*, 119−145. (c) Pillion, J. E.; Thompson, M. E. *Chem. Mater*. **1991**, *3*, 777−779. (d) Enzel, P.; Bein, T. *Chem. Mater.* **1992**, *4*, 819−824. (d) Nazar, L. F.; Zhang, Z.; Zinkweg, D. *J. Am. Chem. Soc*. **1992**, *114*, 6239−6240. (e) Wu, C.-G.; Bein, T. *Science* **1994**, *266*, 1013−1015.

(3) (a) Kanatzidis, M. G.; Tonge, L. M.; Marks, T. J. *J. Am. Chem. Soc.* **1987**, *109*, 3797−3799. (b) Kanatzidis, M. G.; Wu, C.-G. ; Marcy, H. O.; Kannewurf, C. R. *Adv. Mater*. **1990**, *2*, 364−366. (c) Kanatzidis, M. G.; Wu, C.-G.; Marcy, H. O.; DeGroot, D. C.; Kannewurf, C. R. *Chem. Mater.* **1990**, *2(3)*, 222−224.

(4) (a) Yano, K.; Usuki, A.; Okada, A.; Kurauchi, T.; Kamigaito, O. *Polym. Prepr.* **1991**, *32*, 65. (b) Okada, A.; Fukumori, K.; Usuki, A.; Kojima, Y.; Kurauchi, T.; Kamigaito, O. *Polym. Prepr.* **1991**, *32*, 540. (c) Okada, A.; Kawasumi, M.; Usuki, A.; Kojima, Y.; Kurauchi, T.; Kamigaito, O. *Mater. Res. Soc. Symp. Proc.* **1990**, *171*, 45−50 (d) Yano, K.; Usuki, A.; Okada, A.; Kurauchi, T.; Kamigaito, O. *Polym. Prepr.* **1991**, *32*, 65. (e) Okada, A.; Fukumori, K.; Usuki, A.; Kojima, Y.; Kurauchi, T.; Kamigaito, O. *Polym. Prepr.* **1991**, *32*, 540.

(5) (a) Bouhaouss, A.; Aldebert, P. *Mater. Res. Bull* **1983**, *18*, 1247−1256. (b) Casal, B.; Ruiz-Hitzky, E.; Crespin, M.; Tinet, D.; Galvan, J. C. *J. Chem. Soc., Faraday Trans.* **1989**, *86*, 4167−4177. (c) Masbah, H.; Tinet, D.; Crespin, M.; Erre, R.; Setton, R.; Van Damme, H. *J. Chem. Soc., Chem. Commun*, **1985**, 935−936. (d) Erre, R.; Masbah, H.; Crespin, M.; Van Damme, H.; Tinet, D. *Solid State Ionics* **1990**, *37*, 239−251.

(6) (a) Kanatzidis, M. G.; Wu, C.-G.; Marcy, H. O.; Kannewurf, C. R. *J. Am. Chem. Soc*. **1989**, *111*, 4139−4141. (b) Wu, C.-G.; Kanatzidis, M. G.; Marcy, H. O.; DeGroot, D. C.; Kannewurf, C. R. *Polym. Mater. Sci. Eng.* **1989**, *61*, 969−973.

(7) (a) Liu, Y.-J.; DeGroot, D. C.; Schindler, J. L.; Kannewurf, C. R.; Kanatzidis, M. G. *Chem. Mater*. **1991**, *3*, 992−994. (b) Liu, Y.-J.; DeGroot, D. C.; Schindler, J. L.; Kannewurf, C. R.; Kanatzidis, M. G. *Adv. Mater*. **1993**, *5*, 369−372.

(8) *Polymer Electrolyte Reviews*; McCallum, J. R., Vincent, C. A., Eds.; Elsevier Applied Science: London, 1987, 1989; Vols. 1 and 2.

0897-4756/96/2808-0525$12.00/0

various salts have been extensive.[9] However, studies of the PEO complexes inside a constrained environment such as the galleries of various two-dimensional (2-D) inorganic hosts are comparatively rare.[10−12] PEO intercalation has also been reported in phyllosilicates containing Li^+ and Na^+ ions.[10,12] The resulting materials show higher ionic conductivities than those for the parent alkali-exchanged silicates. Direct PEO intercalation can be accomplished in certain aluminosilicate clays using molten polymer.[12a] PEO has also been claimed to insert in layered transition-metal chalcogenides, MPS_3 (M = Mn, Cd) and TaS_2.[11,13] Recently, encapsulation of PEO into MoS_2 was accomplished by taking advantage of the exfoliation property of this dichalcogenide. The resulting intercalation compounds show high electrical conductivity (0.1 S/cm) and metal-to-insulator transitions.[14]

Preliminary results for $(PEO)_{0.5}V_2O_5{\cdot}nH_2O$ phases have been reported earlier.[7a] The composite material showed interesting photosensitivity and could accept Li^+ ions in the framework by the redox reaction with LiI. Further investigation led to the synthesis of several PEO/V_2O_5 phases with additional polymer loading. Here, we report, in detail, the synthesis, structural characterization and chemical, physical, and charge-transport properties of the these materials as a function of PEO loading. The insertion of Li^+ in the $(PEO)_xV_2O_5{\cdot}nH_2O$ phases and their physicochemical characterization is also reported in detail. The behavior of Li^+ ions in the lattice was probed by variable-temperature ^7Li NMR spectroscopy.

Experimental Section

Synthesis. Poly(ethylene oxide), with molecular weights (MW) of 1×10^5 and 5×10^6, was used.

Preparation of V_2O_5 Xerogel. V_2O_5 xerogel was prepared by a reported method.[15] Sodium metavanadate (4 g, 32.8 mmol) was dissolved in 250 mL of distilled water. The resulting solution was eluted through a column packed with H^+ ion-exchange resin (Dowex-50 × 2−100) forming a pale orange solution HVO_3. Upon standing, the HVO_3 polymerized to a red V_2O_5 gel in several days. After evaporation of excess water, a film of V_2O_5 xerogel was formed.

Preparation of $(PEO)_xV_2O_5{\cdot}nH_2O$. Aqueous solutions of 0.01 M V_2O_5 gels were mixed with a stoichiometric amount of PEO (MW = 1×10^5) and stirred overnight in the dark. The PEO/V_2O_5 molar ratio was varied from 0.5 to 5.0 in increments of 0.5. The resulting red mixture was cast into a film by evaporation of water at room temperature on a flat surface without further washing. High molecular weight PEO (MW = 5×10^6) was also used and gave rise to similar intercalation compounds. Therefore, most data in this paper are from low molecular weight PEO.

Photoreaction of $(PEO)_xV_2O_5{\cdot}nH_2O$. A medium-pressure Hg lamp filtered by Pyrex glass was used as a light source. $PEO_xV_2O_5{\cdot}nH_2O$ films, coated on a glass slide, were exposed to this light source in air for 12 h.

Preparation of $Li_y(PEO)_xV_2O_5{\cdot}nH_2O$. An amount of 0.5 g of $PEO_xV_2O_5$ film reacted with 2 equiv of LiI in CH_3CN for 3 days. The resulting blue product was washed with CH_3CN and dried in air. No trace of iodine or iodide were detected in the product by SEM/EDS microprobe analysis. The compositions of these materials were determined by elemental analysis.

Measurements. Infrared spectra were collected from 4000 to 400 cm^{-1} with a resolution of 4 cm^{-1} on a Nicolet 740 FT-IR spectrometer. Samples were recorded, under N_2 flow, in pressed KBr matrixes or as free-standing films.

X-ray diffraction was carried out on a Rigaku rotating anode X-ray powder diffractometer, Rigaku-Denki/RW400F2 (Rotaflex), at 45 kV and 100 mA with a scintillation counter detector and a graphite monochromator to yield Cu Kα (wavelength 1.541 84 Å) radiation. Data were collected at room temperature over the range $2° \le 2\theta \le 100°$ in increments of 0.01°. $\theta/2\theta$ scans were used. Samples were directly coated on X-ray sample slides for reflection mode measurements. For transmission mode measurements, composite films were taped on a sample slide with a hole in the center. The sample slide was placed perpendicular to the X-ray beam and the detector collected data from 2° to 60° in 2θ with a speed of 1°/min. The coherence length was determined from the half-width of peaks using the Scherrer formula:[16]

$$L_{hkl} = K\lambda/B \cos\theta$$

L is the coherence length along the Miller indices (hkl), λ is the X-ray wavelength used, K is Scherrer's constant and has a value of 0.9, θ is the Bragg angle, and B is the peak width at half-height in radians.

Thermogravimetric analysis (TGA) was performed on a Shimadzu TGA-50. Typically 5−10 mg of sample was heated in a quartz crucible in air from room temperature to 1000 °C at the rate of 5 °C/min.

Electron paramagnetic resonance (EPR) spectroscopy was obtained with a Varian E-4 spectrometer operating at 9.5 GHz (X band) and at room temperature. Solid samples were scanned from 2700 to 3700 G at 8 G field modulation and 0.03 s time constant. The g value was obtained with reference to the standard diphenylpycrilhydrazine (DPPH).

Magnetic susceptibility measurements were done on a MPMS Quantum Design SQUID system (superconducting quantum interference device) with a magnetic field of 5000 G. A known quantity of sample was placed in a plastic bag and purged with Ar gas. Data were collected with an ascending ramp from 5 to 300 K and then corrected for the diamagnetic components which were obtained from the literature.[17]

Scanning electron microscopy (SEM) was done with JEOL-JSM 35 CF microscope at an accelerating voltage of 20 kV. Samples were glued to the microscopic sample holder with conducting graphite paint.

Direct-current electrical conductivity and thermopower measurements were performed in the usual four-probe geometry with 60 and 25 mm gold wires used for the current and voltage electrodes, respectively.[18] Thermoelectric power measurements were made by using a slow ac technique with 60 μm gold wires serving to support and conduct heat to the

(9) (a) Hardy, L. C.; Shriver, D. F. *J. Am. Chem. Soc*. **1986**, *108*, 2887. (b) Cameron, G. G.; Ingram, M. D.; Harvie, J. L. *Faraday Discuss.* **1989**, *88*, 55.

(10) (a) Ruiz-Hitzky, E.; Aranda, P. *Adv. Mater*. **1990**, *2*, 545−547. (b) Ruiz-Hitzky, E.; Aranda P.; Casal, B. *J. Mater. Chem*. **1992**, *2(5)*, 581−582. (c) Aranda, P.; Ruiz-Hitzky, E. *Chem. Mater*. **1992**, *4*, 1395−1403.

(11) Lagadic, I.; Léaustic, A.; Clément, R. *J. Chem. Soc., Chem. Commun*. **1992**, 1396−1397

(12) (a) Vaia, R. A.; Vasudevan, S.; Krawiec, W.; Scanlon, L. G.; Giannelis, E. P. *Adv. Mater.* **1995**, *7*, 154−1156. (b) Messersmith, P. B.; Giannelis, E. P. *Chem. Mater.* **1994**, *6*, 1719−1725. (c) Vaia, R. A.; Ishii, H.; Giannelis, E. P. *Chem. Mater.* **1993**, *5*, 1694−1696. (d) Wu, J.; Lerner, M. M. *Chem. Mater.* **1993**, *5*, 835−838.

(13) (a) Ruiz-Hitzky, E.; Jimenez, R.; Casal B.; Manriquez, V.; Ana, A. S.; Gonzalez, G. *Adv. Mater*. **1993**, *5(10)*, 738−741. (b) Lemmon, J. P.; Lerner, M. M. *Chem. Mater.* **1994**, *6*, 207−210.

(14) (a) Bissessur R.; Kanatzidis, M. G.; Schindler, J. L.; Kannewurf, C. R. *J. Chem. Soc., Chem. Commun*. **1993**, 1582−1585. (b) Bissessur, R.; Schindler, J. L.; Kannewurf, C. R.; Kanatzidis, M.G. *Mol. Cryst. Liq. Cryst.* **1993**, *245*, 249−254.

(15) Lemerle, J.; Nejem, L.; Lefebvre, J. *J. Inorg. Nucl. Chem*. **1980**, *42*, 17−20.

(16) Klug, H. P.; Alexander, L. E. *X-ray Diffraction Procedures for Polycrystalline and Amorphous Materials*; John Wiley & Sons: New York, 1962; 491−538.

(17) Boudreaux, E. A.; Mulay, L. N. *Theory and Applications of Molecular Paramagnetism*; John Wiley & Sons: New York, 1976.

(18) Lyding, J. W.; Marcy, H. O.; Marks, T. J.; Kannewurf, C. R. *IEEE Trans. Instrum. Meas.* **1988**, *37*, 76−80.

sample, as well as to measure the voltage across the sample resulting from the applied temperature gradient.[19]

Optical diffuse reflectance spectra were measured at room temperature with a Shimadzu UV-3101PC double beam, double monochromator spectrophotometer. Samples were placed above $BaSO_4$ on a sample holder. $BaSO_4$ powder was used as a reference. The absorption spectrum was calculated from the reflectance data using the Kubelka−Munk function: $\alpha/S = (1 - R)^2/2R$. R is the reflectance, α is the absorption coefficient, and S is the scattering coefficient which is practically wavelength independent when the particle size is larger than 5 μm.[20]

^{7}Li NMR spectra were recorded on a Varian 400 MHz instrument using a wide-line Varian probe equipped with a variable-temperature (VT) control, at a frequency of 155.45 MHz. All samples were run with a repetition delay time of 1 s with typical 90° pulse of 2.8 μs.

One-dimensional Patterson function and electron density (ED) calculations were based on the X-ray reflection data. Six 00l reflections were used for the V_2O_5 xerogel out to d_{008} = 1.43 Å, 10 reflections were used for $(PEO)_{0.5}V_2O_5{\cdot}nH_2O$ out to d_{0010} = 1.35 Å, 12 reflections were used for $(PEO)_{1.0}V_2O_5{\cdot}nH_2O$ out to d_{0013} = 1.34 Å and 11 reflections were used for $(PEO)_{1.5}V_2O_5{\cdot}nH_2O$ out to d_{0012} = 1.42 Å. The intensities were obtained from the integrated peak areas. The structure factors, F, of these reflections were derived from their intensities and corrected by Lorentz-polarization effects according to eqs 1 and 2.

$$|F(l)| = (I/Lp)^{1/2} \tag{1}$$

$$Lp = (1 + \cos^2 2\theta)/(\sin^2 \theta \cos \theta) \tag{2}$$

where I is the peak intensity and Lp is the Lorentz-polarization factor. The observed $|F(l)|^2$ values for $V_2O_5{\cdot}nH_2O$, $(PEO)_{0.5}V_2O_5{\cdot}nH_2O$, $(PEO)_{1.0}V_2O_5{\cdot}nH_2O$, and $(PEO)_{1.5}V_2O_5{\cdot}nH_2O$, were used to calculate 1-D Patterson functions according to eq 3. The functions were synthesized from z = 0.0 to 1.0 in increments of 0.01 for all materials.

$$P(z) = 2/c \sum_l |F(l)|\ 2\cos(2\pi/z) \tag{3}$$

The signs (phases) of the structure factors were directly obtained from the scattering contributions of the V_2O_5 framework. This reasonably assumes that the scattering contribution from the intercalated PEO is relatively small. Atomic scattering factors for vanadium and oxygen were determined by eq 4, where the values of a_i, b_i, and c for each element were

$$f(\theta) = [\sum_{i=1}^{4} a_i \exp(-b_i\lambda^{-2} \sin^2 \theta) + c] \exp\left(-\frac{B \sin^2 \theta}{\lambda^2}\right) \tag{4}$$

obtained from the literature.[21] B is a temperature factor and for simplicity is set at 2.0 A^2 for every atom. The structure factors were calculated according to eq 5, where f_j is the

$$F(l) = \sum_{j=1}^{N} 2f_i \cos(2\pi/z_i) \tag{5}$$

scattering factor of j atom (obtained from eq 4), l is a Miller index, and z_j is its fractional coordinate on the c axis. Here,

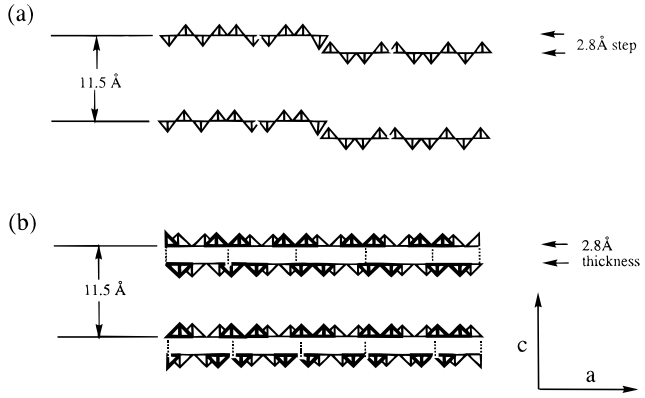

Figure 1. Schematic illustration of the proposed structure of V_2O_5 xerogel projected onto the *ac* plane: (a) from Livage et al.; (b) from Oka et al.

Oka's model was used (see Figure 1).[22] The 1-D electron densities were obtained from eq 6. L is the length of the repeat

$$\rho(z) = (1/L)[F_0 + 2\sum_l F_l \cos(2\pi/z)] \tag{6}$$

unit and F_0 is the zeroth-order structure factor. The electron density maps of the PEO/V_2O_5 materials were calculated by using the $|F(l)|_{obsd}$, obtained from eq 1, with the signs obtained based on the V_2O_5 part of the structure. The electron density maps were synthesized from $z = -0.2$ to 1.2 in increments of 0.01. The signs of the phases were also checked by recalculation of the electron densities, including the scattering contributions of the PEO molecules. In this calculation, the exact amounts of PEO molecules (based on elemental analysis) with the different possible conformations and positions were used. Before and after the PEO molecules were included, the signs of the phases were consistent in the case of $(PEO)_{1.0}V_2O_5{\cdot}nH_2O$. Only one reflection changed sign in $(PEO)_{1.5}V_2O_5{\cdot}nH_2O$, but this did not consequently change the ED pattern.

Results and Discussion

Structure of V_2O_5 Xerogel. Besides the fact that V_2O_5 xerogel is known to be lamellar, with an interlayer distance of 11.5 Å, its actual structure remains an unresolved issue. Livage et al. proposed that the V_2O_5 layers are composed of corrugated ribbons with a step of 2.8 Å,[23] with the intraribbon structure being closely related to the layers of orthorhombic V_2O_5, see Figure 1a. Recently, Oka et al. proposed a different structure in which the layers consist of two V_2O_5 sheets facing each other at a distance of 2.8 Å according to the structure of $A_xV_2O_5$[22] (A = Na, K); see Figure 1b. Most studies reported to date seem to prefer Livage's model.[2,23] However, density measurements for $V_2O_5{\cdot}1.08$DMSO and $(PEO)_{1.0}V_2O_5{\cdot}0.7H_2O$, shown in Table 1, are consistent with Oka's model. Interestingly, neither model can fully index the observed (hk0) reflections from the X-ray diffraction pattern obtained in transmission geometry. These are the reflections which derive from the in-plane structure of $V_2O_5{\cdot}nH_2O$.

Characterization of $(PEO)_xV_2O_5{\cdot}nH_2O$ Phases. A series of $(PEO)_xV_2O_5{\cdot}nH_2O$ nanocomposite intercalates with $0.5 < x < 5.0$ were prepared. X-ray diffraction

(19) Marcy, H. O.; Marks, T. J.; Kannewurf, C. R. *IEEE Trans. Instrum. Meas.* **1990**, *39*, 756−760.

(20) (a) Wendlandt, W. W.; Hecht, H. G. *Reflectance Spectroscopy*; Interscience Publishers: New York, 1966. (b) Kotüm, G. *Reflectance Spectroscopy*; Springer-Verlag: New York, 1969. (c) Tandon, S. P.; Gupta, J. P. *Phys. Status. Solidi* **1970**, *38*, 363−367.

(21) *International Tables for X-ray Crystallography*; The Kynoch Press: English, 1974.

(22) (a) Yao T.; Oka,Y.; Yamamoto, N. *Mater. Res. Bull.* **1992**, *27*, 669−675. (b) Yao T.; Oka,Y.; Yamamoto, N. *J. Mater. Chem.* **1992**, *2*, 331−336. (c) Yao T.; Oka,Y.; Yamamoto, N. *J. Mater. Chem.* **1992**, *2*, 337−340.

(23) (a) Legendre, J.-J.; Livage, J. *J. Colloid Interface Sci.* **1983**, *94*, 75−83. (b) Livage, J. *Chem. Mater.* **1991**, *3*, 573−593.

Table 1. Calculated and Measured Densities for $(DMSO)_{1.08}V_2O_5$ and $(PEO)1.0V_2O_5{\cdot}0.7H_2O$

compound	calc density (g/cm^3)		
	Livage model	Oka model	measd value
V2O5·1.08DMSO[a]	1.18	2.35	2.25
(PEO)1.0V_2O_5·0.7H^{2}O	1.1	−2.2	−2.3

[a] From ref 22.

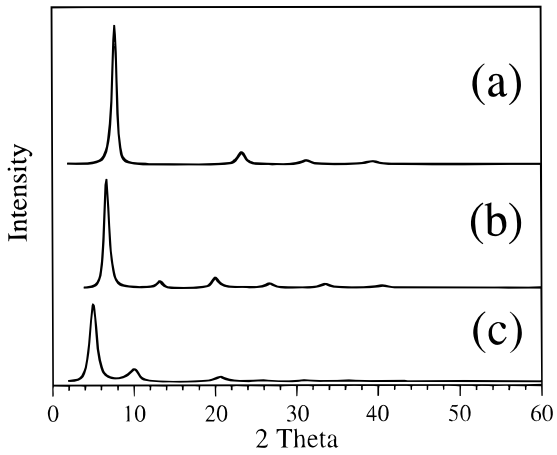

Figure 2. X-ray powder diffraction patterns (reflection mode) of films of (a) V_2O_5 xerogel, (b) $(PEO)_{0.5}V_2O_5{\cdot}nH_2O$, and (c) $(PEO)_{1.5}V_2O_5{\cdot}nH_2O$.

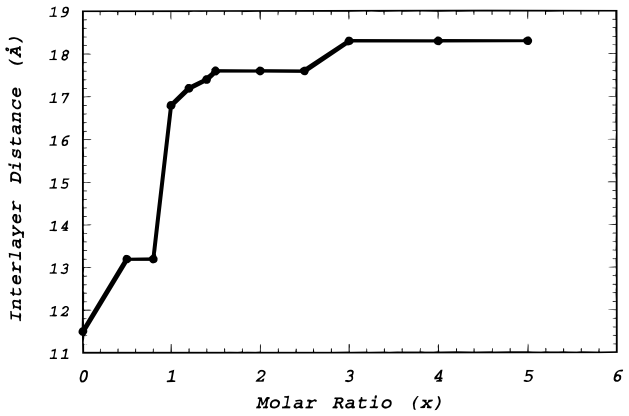

Figure 3. Variation of interlayer spacing as a function of polymer loading (i.e., x) in $(PEO)_xV_2O_5{\cdot}nH_2O$.

patterns from film samples clearly show that the 00l reflections dominate, see Figure 2. The phase with $x = 0.5$ has an interlayer spacing of 13.2 Å, and as x increases, the interlayer distance increases to 16.8 Å at $x = 1.0$ and to 18.3 Å at $x = 5$; see Figure 3 and Table 2. The net V_2O_5 interlayer expansion is from 4.5 Å at $x = 0.5$ to 9.6 Å at $x = 5.0$. The stacking regularity primarily decreases with higher polymer loading according to the coherence length measured (with Scherrer formula) along the layer stacking direction which decreases from 90 Å when $x = 0.5$ to 60 Å when $x = 4$. Scanning electron micrographs of the PEO/V_2O_5 composites clearly show that after intercalation, the surface becomes distinctly corrugated, consistent with increased disorder; see Figure 4. Compared with V_2O_5 xerogel, however, these composite films show much improved mechanical flexibility which becomes more noticeable as the PEO content increases. The films can be bent or rolled readily but break when press-folded. All of the phases absorb moisture reversibly, which causes a further 2 Å expansion in the interlayer distance. However, these highly hydrated forms of $(PEO)_xV_2O_5{\cdot}nH_2O$

Table 2. Summary of Interlayer Distance, Net Expansion, and Coherence Length for $(PEO)_xV_2O_5.nH_2O$[a]

molar ratio (PEO/V_2O_5)	interlayer distance (Å)	net expansion[b] (Å)	coherence length[c] (Å)
0*	11.5	2.8	100
0.5	13.2	4.5	90
0.8	13.2	4.5	90
1.0	16.8	6.9	88
1.2	17.2	8.5	70
1.4	17.4	8.7	77
1.5	17.6	8.9	75
2.0	17.6	8.9	75
2.5	17.6	8.9	70
3.0	∼18.3	9.6	65
4.0	∼18.3	9.6	60
5.0	∼18.3	9.6	60

[a] n is ∼1−1.6 for the phases with $x < 1$ and 0.5−1.0 for the phases with $x \geq 1$. [b] The thickness of the V_2O_5 layer is 8.7 Å. [c] Along the layer stacking axis. [d] V_2O_5 xerogel.

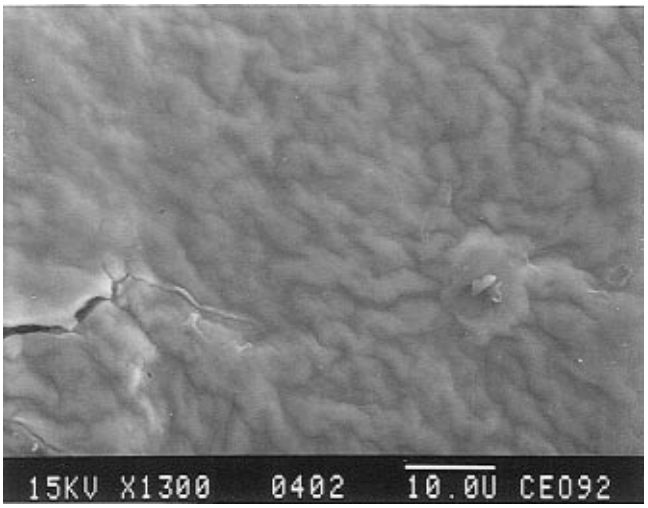

Figure 4. SEM photographs of $(PEO)_{1.5}V_2O_5{\cdot}nH_2O$.

are more disordered and sometimes consist of mixed phases. Materials with high MW PEO (5.0×10^6) were also prepared, and they generally show an improved structural order in the layer stacking direction. For example, the coherence length of $(PEO)_{0.5}V_2O_5{\cdot}nH_2O$ increases to 112 Å, a value higher than that of V_2O_5 xerogel itself.

Despite the large amounts of PEO that can be intercalated in the xerogel, when $x > 2.5$, a considerable amount of polymer exists outside the layers as a separate phase. The excess PEO can be washed away with CH_3CN, but this treatment always removes some intercalated PEO, especially when $x > 2.5$, giving products with $x \sim 2.0$. The interlayer spacing also decreases after such washings from 18.3 to 17.5 Å. Thus, we were not able to precisely determine the maximal PEO loading in the V_2O_5 framework from these experiments. FT-IR spectroscopy and X-ray diffraction indicate that an accumulation of the bulk PEO phase begins from $x > 2.5$ despite the fact that additional PEO continues to enter the V_2O_5 galleries.

PEO intercalation does not affect the structural integrity of the V_2O_5 framework as confirmed by X-ray diffraction and infrared spectroscopic data. Because of preferred orientation of the PEO/V_2O_5 composite films on flat substrates, X-ray diffraction in reflection mode only contains the 00l set of reflections. The $hk0$ and hkl sets, which derives from the in-plane structure, can be only observed in the transmission mode. The trans-

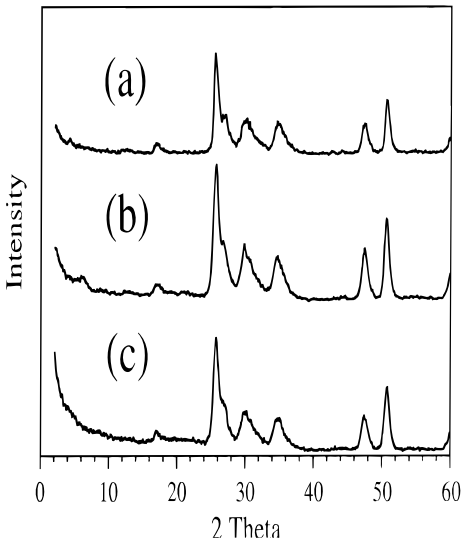

Figure 5. Transmission mode of X-ray diffraction patterns for (a) V_2O_5 xerogel, (b) $(PEO)_{0.5}V_2O_5{\cdot}nH_2O$, and (c) $(PEO)_{1.5}V_2O_5{\cdot}nH_2O$.

mission diffraction patterns of all PEO/V_2O_5 phases are identical with that of the pristine V_2O_5 xerogel, confirming that the intercalation is topotactic; see Figure 5. All products show three strong framework vibrations at 1010, 750, and 570 cm^{-1} and two intense electronic transitions at 270 and 380 nm, due to oxide-to-metal charge transfer. These values are nearly identical with those of V_2O_5 xerogel; however, the intercalated PEO shows some structural modifications relative to bulk. In the CH_2 stretching absorption region, the strong band at 2880 cm^{-1} and two weak bands at a slightly higher energy, observed in bulk PEO, change into two well-defined bands at 2910 and 2878 cm^{-1}. In the region 1500−1100 cm^{-1}, no significant energy shifts are observed with respect to bulk PEO, but the relative intensities between absorptions are different and the band shapes become broader. Below 1100 cm^{-1}, the absorptions are mainly shielded by the strong vibrations of the V_2O_5 framework. These small but significant changes are due to steric interactions between the confined polymer and the framework and suggest conformational differences between the intercalated and bulk forms of PEO.

Structure of $(PEO)_xV_2O_5{\cdot}nH_2O$. The relatively large number of 00*l* reflections observed in some samples allowed us to probe the structure of the intercalated species, projected on the *c* axis, via Fourier transform analysis. This is possible by calculating one-dimensional Patterson functions and electron-density maps from the observed intensities. On the basis of the structural model available for the vanadium oxide part of the structure, the projection of the PEO structure on the *c* axis may be determined from difference electron-density maps. This could yield specific information about the orientation and structure of the intercalated polymer or at least eliminate certain conformational possibilities which are incompatible with the diffraction data. For the purposes of this study, accurate knowledge of the in-plane structure of V_2O_5 xerogel is not necessary, because both the Livage as well as the Oka models give identical projections on the *c* axis. The one-dimensional Patterson functions, calculated from the 00*l* reflections, are shown in Figure 6. The 1-D Patterson function of V_2O_5 xerogel itself shows two peaks at 2.8 and 4.5 Å.[24] The strong peak at 2.8 Å is assigned to the V−V vector (projected on the c-axis) from the V_2O_5 layers and the peak at 4.5 Å is due to the V−O vector involving oxide atoms and water.[23,24] These PEO intercalates preserve the original Patterson peaks associated with the V_2O_5 framework and show a new broad peak centered at 6.6 Å for $(PEO)_{0.5}V_2O_5{\cdot}nH_2O$ and 8.8 Å for $(PEO)_{1.5}V_2O_5{\cdot}nH_2O$. Its intensity increases with PEO loading, indicating that the peak is due to the vector between vanadium atoms and atoms in PEO. The appearance of these peaks independently confirms that the internal structure of the V_2O_5 layers is intact and indicates that PEO is positioned in interlayer regions and not at intralayer regions. This point is important in the following 1-D electron density calculations which probe the PEO conformation.

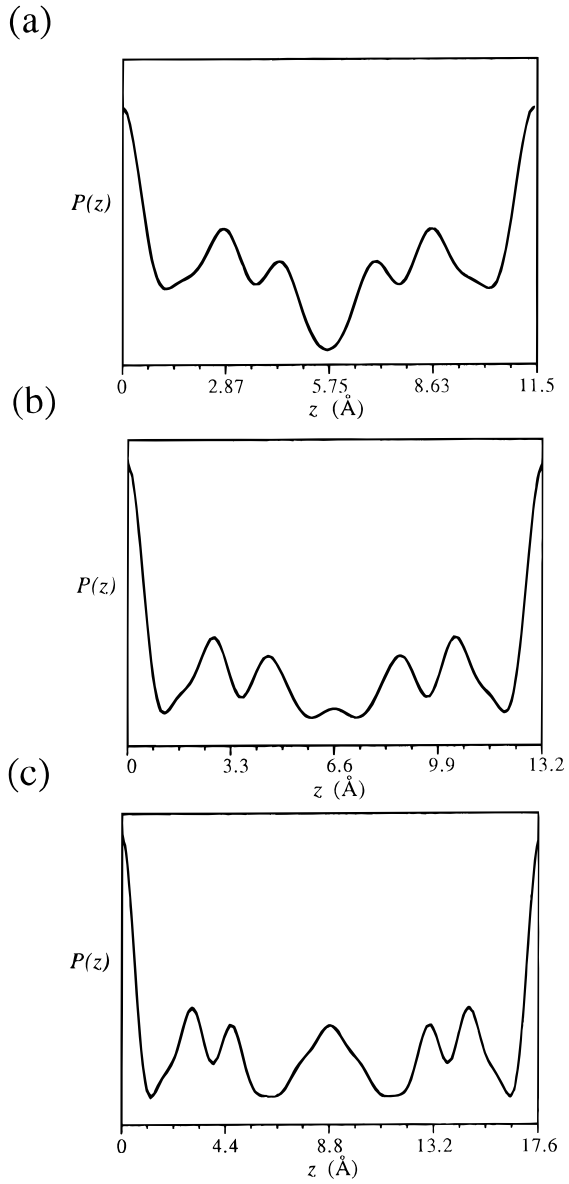

Figure 6. One-dimensional Patterson functions along the interlayer *c* axis of (a) V_2O_5 xerogel, (b) $(PEO)_{0.5}V_2O_5{\cdot}nH_2O$, and (c) $(PEO)_{1.5}V_2O_5{\cdot}nH_2O$.

That the interlayer expansion as a function of PEO content does not vary linearly but shows plateaus

(24) Legendre, J.-J.; Aldebert, P.; Baffier, N.; Livage, J. *J. Colloid Interface Sci.* **1983**, *94*, 84−89.

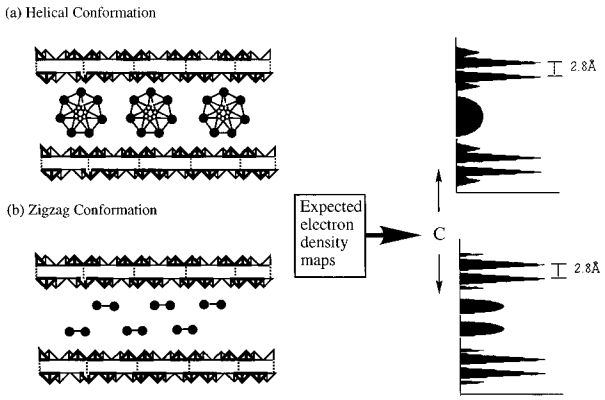

Figure 7. Schematic structures of PEO conformation in the V_2O_5 framework and their expected electron density projections along the *c* axis (depicted from Oka's model). (a) Coil conformation with rotational disorder about the helical axis. In this case the projection of the individual C and O atoms is poorly resolved. (b) Fully extended plana-zigzag conformation. In both cases the polymer extends perpendicular to the figure.

(Figure 3) suggests that the intercalation of PEO is either a complicated layer-by-layer process or subject to a conformational change from a fully extended planar zigzag to a helix. For example, $(PEO)_{0.5}V_2O_5{\cdot}nH_2O$ has a net expansion of only 4.5 Å which is too small for a helical structure and more consistent with a planar zigzag conformation. However, $(PEO)_xV_2O_5{\cdot}nH_2O$ phases with $x \geq 1$ have a net expansion of 8 Å or higher, and this is compatible with either two layers of polymer chains with a planar zigzag conformation, or one layer of helical PEO. To probe the polymer conformation, 1-D electron density (ED) maps were calculated along the *c* axis.

If PEO adopted a coil conformation, the 1-D ED map along the *c* axis would be expected to show a broad feature, made of poorly resolved peaks, disposed halfway between the peaks of the V_2O_5 layers; see Figure 7a. If PEO, however, had a straight-chain planar-zigzag conformation, the 1-D ED map can show several different patterns which depend on the packing arrangement of the polymer chains. For example, if the molecular plane is parallel to the V_2O_5 layer, then a bilayer model is needed to explain the 8 Å expansion and the 1-D ED map should show two peaks (roughly ~4 Å apart) symmetrically disposed from the middle of the gallery; see Figure 7b. On the other hand, if the polymer plane is perpendicular to the V_2O_5 sheet, the 1-D ED map should show four peaks each for a single polymer chain; see Figure 8a. In this case, the distance between peaks should be less than 0.9 Å. Yet another possibility is that the PEO bilayer structure is arranged in a corrugated fashion. In this case too, four electron density peaks with distances between them being ~1 to ~2 Å are expected; see Figure 8b. Of course, there are still other more elaborate but less likely possibilities. A 1-D ED calculation of the $(PEO)_{1.0}V_2O_5{\cdot}nH_2O$ phase, based on Oka's model, is shown in Figure 9. As expected, the projection of this structure on the *c* axis gives rise to two strong peaks, one at ~2.8 Å, which is due to the distance between the two vanadium planes, and another at ~1.6 Å which is due to the projection of the V=O bonds. Four additional peaks due to PEO are observed between the layers and are spaced ~ 2.0 Å apart. This eliminates the helical coil structure and suggests that the intercalated PEO chains are fully extended and

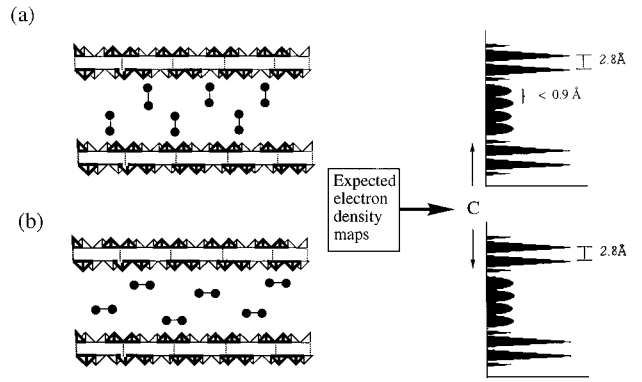

Figure 8. Two schematic arrangements of planar-zigzag PEO chains in the V_2O_5 framework and their expected electron density projections along the *c* axis: (a) the plane containing the polymer chain is perpendicular to the V_2O_5 sheet and (b) the plane is parallel to the V_2O_5 sheet, and the PEO bilayer arrangement is in a zigzaglike fashion.

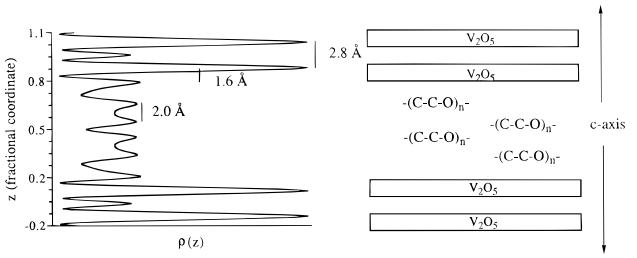

Figure 9. Projection of the electron density of $(PEO)_{1.0}V_2O_5{\cdot}nH_2O$ and illustrations of the deduced arrangement of PEO in the interlayer space.

parallel to each other arranged in a bilayer fashion alternating above and below the 002 plane; see Figure 8b. The straight-chain conformation suggested here contrasts the coil conformation claimed in other systems containing alkali ions.[25] An additional strong argument against the coil structure comes from the fact that such a conformation would expose a hydrophobic polymer surface (i.e., mostly of CH_2 groups) to the hydrophilic $V_2O_5{\cdot}nH_2O$ environment while hiding the oxygen atoms in the center of the coil. This arrangement would minimize hydrogen bonding between the host and the guest and would be destabilizing.

At low PEO levels, the driving force for PEO/V_2O_5 stabilization seems to be van der Waals interactions and hydrogen bonding which are maximized when the polymer is fully extended (i.e., zigzag conformation). Corresponding 1-D ED maps for $(PEO)_{1.5}V_2O_5{\cdot}nH_2O$ show a similar pattern to $(PEO)_{1.0}V_2O_5{\cdot}nH_2O$, indicating that the intercalated PEO molecules in both compounds are arranged similarly. The results presented here suggest that the PEO intercalation is a layer-by-layer insertion without any conformational change from a zigzag to a helix. Similar calculations for phases with $x > 1.5$ were not performed due to low crystallinity and insufficient numbers of observed reflections. Attempts to incorporate Li salts such as $LiClO_4$ and $LiCF_3SO_3$ during the preparation of $(PEO)_xV_2O_5{\cdot}nH_2O$ did not succeed. On the basis of the X-ray diffraction, the product is a mixture of V_2O_5 and/or PEO/V_2O_5 as well as a Li salt complex of PEO.

Irradiation-Induced Internal Electron Transfer in $(PEO)_xV_2O_5{\cdot}nH_2O$. The $(PEO)_xV_2O_5{\cdot}nH_2O$ materi-

(25) Ruiz-Hitzky, E.; Casal, Blanca *J. Chem. Soc., Faraday Trans. 1* **1986**, *82*, 1597−1604.

Table 3. X-ray Diffraction and Magnetic Data for Irradiated $(PEO)_xV_2O_5{\cdot}nH_2O$ Compounds

x	color	d-spacing contraction (Å)	EPR (G)	μ_{eff}[c] (μ_B)	$\chi_{(TIP)}$[b] (emu/mol)
0.5	blue	0.2	400[a]	0.73	1.28×10^{-4}
1.0	blue	2.2	hyperfine structure	0.81	1.55×10^{-4}
1.5	blue	1.2	hyperfine structure	0.77	1.36×10^{-4}

[a] Peak-to-peak width. [b] TIP: temperature-independent paramagnetism. [c] μ_{eff} was calculated from the $\chi_{Curie-Weiss}$ component.

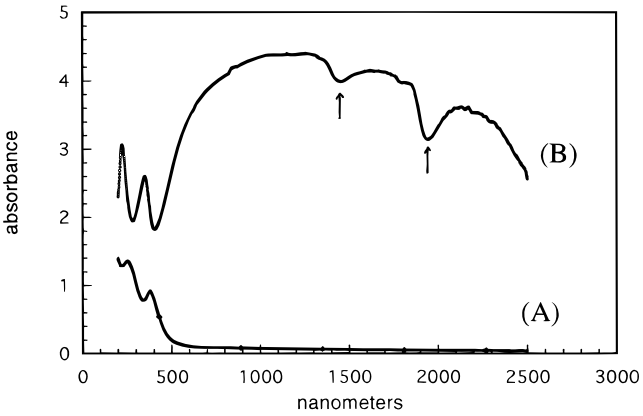

Figure 10. Optical absorption spectra of (A) unirradiated and (B) irradiated $(PEO)_{0.5}V_2O_5{\cdot}nH_2O$. The features indicated by the arrows are due to the presence of water and are generated when there is a difference in water content between the reference material ($BaSO_4$) and the sample.

als are light-sensitive and turn blue when they stand in room light for several weeks. Exposure to a medium-pressure Hg lamp causes the materials to turn blue in an hour. The color change is due to a light-induced redox reaction in which the PEO is oxidized by the vanadium oxide framework. The films lose their mechanical flexibility and become brittle. The infrared spectra of irradiated samples show a new very weak absorption around 1700 cm^{-1}, indicating that the PEO chains are oxidized to shorter ones with aldehyde, ester, or even carboxylic acid end groups. The vibration of V=O slightly shifts lower to ~1000 cm^{-1}, consistent with an increased number of V^{4+} centers. Except for these, we do not observe significant changes in the position and shape of infrared absorption peaks of the PEO and vanadium oxide framework, suggesting only minor structural changes in the framework. The irradiation slightly decreases the interlayer spacing (see Table 3), due to water expulsion from the layers because the reduced V_2O_5 framework becomes more hydrophobic.

Optical diffuse reflectance spectra of the irradiated materials show a new very broad absorption band centered at 1400 nm (see Figure 10), which is due to an intervalence electronic transition associated with the mixed valence V^{4+}/V^{5+} framework.[26] The appearance of this band is due to the increased number of V^{4+} centers in the V_2O_5 framework and confirms the charge transfer from the polymer to the V_2O_5 framework.

The redox nature of the photoreaction is also confirmed by the increased magnetic susceptibility and enhanced intensity of the EPR signal of these materials. Figure 11 shows variable-temperature magnetic susceptibility data for fresh and irradiated samples. Although the magnetic susceptibility (χ_m) decreases with rising temperature the data do not obey strict Curie–Weiss law. The magnetic behavior can be best interpreted as Curie–Weiss type with a small amount of van Vleck temperature-independent paramagnetism (TIP).[26,27] The unirradiated PEO/V_2O_5 compounds have an average μ_{eff} (calculated from the $\chi_{Curie-Weiss}$ component of the susceptibility) of ~0.3–0.4 μ_B at room temperature. Continuous irradiation for ~12 h generates additional V^{4+} centers and increases μ_{eff} to 0.7–0.8 μ_B; see Table 3.

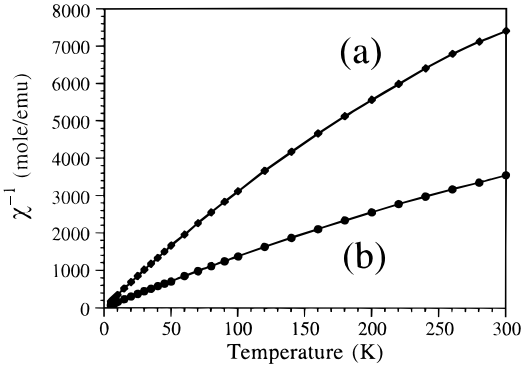

Figure 11. Inverse magnetic susceptibility of (a) fresh and (b) irradiated $(PEO)_{0.5}V_2O_5{\cdot}nH_2O$ as a function of temperature.

Before irradiation, the EPR hyperfine structure is observed in the spectra of PEO/V_2O_5 materials due to $(V{=}O)^{2+}$ impurities ($S = {}^1/_2$, $I = {}^7/_2$) in an axially distorted crystal field.[28,29] Irradiation of $(PEO)_{0.5}V_2O_5{\cdot}nH_2O$ causes a gradual disappearance of the original hyperfine splitting and the appearance of a broad peak at $g \sim 1.96$. The broadening is due to V^{4+}–V^{4+} exchange interactions. Surprisingly, when $x \geq 1$, the EPR spectra of $(PEO)_xV_2O_5{\cdot}nH_2O$ do not change dramatically with irradiation despite the fact that the these materials also get dark blue and show a slightly higher μ_{eff} than that of $(PEO)_{0.5}V_2O_5{\cdot}nH_2O$. The persistence of the EPR hyperfine structure, in irradiated $(PEO)_xV_2O_5{\cdot}nH_2O$ (for $x > 1$) suggests that the average V^{4+} concentration in the layers is lower than that in $(PEO)_{0.5}V_2O_5{\cdot}nH_2O$. One possible explanation for this "paradox" is that some of V^{4+} centers, probably in the form of VO^{2+}, diffuse between the layers and are magnetically isolated by coordination to PEO.[29]

Lithium Ion Insertion. As shown above, the intercalation of PEO does not change the structure and electronic state of V_2O_5 framework, and therefore the $(PEO)_xV_2O_5{\cdot}nH_2O$ compounds preserve the oxidation potential of the V_2O_5 framework and should be good hosts for further redox intercalation. For example, reaction with lithium iodide leads to insertion of Li^+ ions into the PEO/V_2O_5 phases according to eq 7. This reaction reduces the V_2O_5 framework and produces iodine as a byproduct which is detected spectroscopically. The products acquire a blue color and increased

(26) Liu, Y.-J.; Cowen, J. A.; Kaplan, T. A.; DeGroot, D. C.; Schindler, J. L.; Kannewurf, C. R.; Kanatzidis, M. G. *Chem. Mater.* **1995**, *7*, 1616–1624.

(27) (a) Drago, R. S. *Physical Methods in Chemistry*; W. B. Sanders Co.: Philadelphia, 1977. (b) Liu, Y.-J.; Kanatzidis, M. G., manuscript in preparation.

(28) Sanchez, C.; Babonneau, F.; Morineau, R.; Livage, J.; Bullot, J. *Philos. Mag. B* **1983**, *3*, 279–290.

(29) The existence of VO^{2+} species has been proposed in the reduced V_2O_5 xerogels. Babonneau, F.; Barboux, P.; Josien, F. A.; Livage, J. *J. Chim. Phys.* **1985**, *82*, 761–766.

$$y\mathrm{LiI} + (\mathrm{PEO})_x\mathrm{V_2O_5}{\cdot}n\mathrm{H_2O} \rightarrow \mathrm{Li}_y(\mathrm{PEO})_x\mathrm{V_2O_5}{\cdot}n\mathrm{H_2O} + y/2\mathrm{I_2} \quad (7)$$

magnetic susceptibility much like the irradiated products discussed above. The infrared spectra of $Li_y(PEO)_xV_2O_5{\cdot}nH_2O$ show no significant changes from those prior to intercalation. The compositions and interlayer spacings of the $Li_y(PEO)_xV_2O_5{\cdot}nH_2O$ compounds are listed in Table 4. Li insertion decreases the interlayer distance and increases the disorder as judged by the decrease of the average coherence length from ~85 to ~65 Å. Regardless of y the net interlayer height is considerably less than the 8 Å expected for a PEO coil containing Li^+ cations. These data show that the incorporation of Li^+ ions does not change the conformation of PEO from a full extended straight chain structure to a coil. A coil conformation was claimed for the PEO in alkali phyllosilicates.[13]

The environment of the Li^+ ions in the galleries is not known but it is quite likely that they are solvated by water and do not bind to PEO. Alternatively, the bonding mode between the PEO and the Li^+ ions, if any, must be such that a coiled structure is avoided. The net expansion of 7.7 Å in $Li_y(PEO)_{1.5}V_2O_5{\cdot}nH_2O$ is the largest observed in this family of materials but still too small to accommodate a Li-containing coil of PEO. The Li^+ insertion products do not show a sufficient number of 00l reflections in the X-ray pattern to warrant a meaningful electron density calculation as was done above. Thus, the conformation of PEO and the chain arrangement in $Li_y(PEO)_xV_2O_5{\cdot}nH_2O$ could not be probed by this technique.

^{7}Li NMR Spectroscopy. The $Li_y(PEO)_xV_2O_5{\cdot}nH_2O$ materials were examined with variable-temperature wide-line ^{7}Li NMR spectroscopy in the hope of probing the state and coordination of Li^+ in the galleries. For comparison purposes the $Li_{0.20}V_2O_5{\cdot}nH_2O$ was prepared and studied as well. All samples showed just one peak due to a first order quadrupolar transition with no significant satellite peaks. The width at half-height ($\Delta\nu_{1/2}$) generally decreases with rising temperature as shown in Figure 12. Typically, $\Delta\nu_{1/2}$ decreases gradually but slowly with increasing temperature, and then a significant rapid narrowing of the line is observed above 220 K up to 320 K, after which the line narrowing again gradually increases. As long as the temperature remains <350 K, above which the vanadium oxide framework begins to decompose, this "sigmoidal" behavior in the data is reversible for many cooling and heating cycles. The range of temperature over which $\Delta\nu_{1/2}$ changes is influenced by the amount of PEO in the galleries. Even though all intercalates behave similarly, the sample with the lowest PEO content, $Li_{0.18}(PEO)_{0.5}V_2O_5{\cdot}nH_2O$ (I) shows the highest width in the lower temperature region (<240 K).

The spectrum of $Li_{0.2}V_2O_5{\cdot}nH_2O$ undergoes a similar line narrowing at higher temperature; see Figure 12. Interestingly, this sample, which contains the highest lithium content, shows a signal with a broader base at all temperatures, perhaps suggesting different Li^+ sites. At higher temperature a significant amount of asymmetry is also observed while the broader base is retained. The asymmetry of the resonance line in this sample is an indication of several overlapping signals from symmetric and asymmetric Li^+ environments which induce an electric field gradient (efg) around the Li nuclei.

Table 4. Composition, Net Expansion, and Coherence Length of $Li_y(PEO)_xV_2O_5{\cdot}nH_2O$

x	*M*	*y*	net interlayer expansion (Å)	coherence length (along *c* axis) (Å)
0.5	Li	0.18	4.3	76
1.0	Li	0.04[a]	5.4	46
1.5	Li	0.17	7.7	60

[a] Prepared by using large pieces of PEO/V_2O_5 films and no stirring during the reaction.

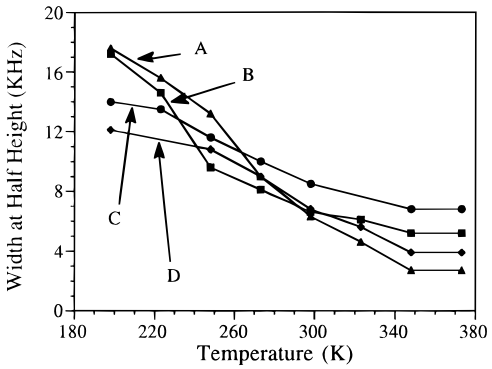

Figure 12. Width at half-height versus temperature for ^{7}Li NMR signals of (A) $Li_{0.18}(PEO)_{0.5}V_2O_5{\cdot}nH_2O$, (B) $Li_{0.2}V_2O_5{\cdot}nH_2O$, (C) $Li_{0.04}(PEO)_{1.0}V_2O_5{\cdot}nH_2O$, and (D) $Li_{0.17}(PEO)_{1.5}V_2O_5{\cdot}nH_2O$.

The sample with the highest PEO load and a comparable amount of Li, $Li_{0.17}(PEO)_{1.5}V_2O_5{\cdot}nH_2O$ (II), shows a much narrower signal below 240 K than does I. Though both samples have similar $\Delta\nu_{1/2}$ at 280 K, at higher temperatures, the situation is reversed and the sample with the highest PEO shows a larger $\Delta\nu_{1/2}$. In both cases the signals are symmetric at all temperatures with no indication of different lithium environments. This suggests that the sites the Li ions can occupy in the galleries are very much affected by the presence of PEO which imposes constrains on Li^+ mobility. The sample with an intermediate PEO load but with the lowest lithium content $Li_{0.04}(PEO)_{1.0}V_2O_5{\cdot}nH_2O$, shows an intermediate line narrowing below 240 K. Thus, below *ca.* 280 K, regardless of the amount of lithium content, the higher the PEO content the wider the ^{7}Li NMR signal. The possible lithium environment in these samples can be divided in several types, one of which would be exclusive coordination to oxygen atoms of PEO. Other kinds of Li environment include a mixed PEO/water coordination and a full water coordination. Of course, it is also possible that framework oxide ions may interact with Li^+, although this is unlikely when PEO and water are present. The distribution of these different Li^+ environments would depend on the PEO/water ratio in the material. For example, in materials with low PEO content the Li may be coordinated primarily to water. Distribution of the Li^+ sites may also depend on the temperature. For example, at higher temperature a more homogeneous lithium environment may be achieved through thermal equilibration and ion hopping. The fact that we observe only one signal at low temperature suggests but does not prove that the Li^+ ions are primarily in one type of environment. The materials exhibiting asymmetric ^{7}Li NMR lines, however, may indeed contain a significant fraction of lithium ions in different sites. The substantial line narrowing observed in the spectra of all materials with increasing

temperature is consistent with enhanced ion mobility and ion-conductivity in these systems. An increase in temperature naturally leads to an increase in the mobility or site-exchange frequency of lithium. Ion mobility will cause changes in the local environment of the Li^+ ions. A similar observation of line narrowing of ^7Li NMR signals with increasing temperature has been reported earlier for $(PEO)_8LiClO_4$ and $Li_{1+x}V_3O_8$.[30] Furthermore, other quadrupolar nuclei like sodium, when complexed to PEO, have been shown to undergo a similar line narrowing transition with temperature.[31]

The spin lattice relaxation time T_1 at room temperature measured by the spin recovery technique shows 117 ms for $Li_{0.18}(PEO)_{0.5}V_2O_5{\cdot}nH_2O$ and 131 ms for $Li_{0.17}(PEO)_{1.5}V_2O_5{\cdot}nH_2O$. These T_1 values are in the same range with values reported earlier for Li salts of PEO.[32] The larger T_1 in the latter material suggests that the relaxation of lithium is influenced by the amount of PEO in the layer and may reflect a greater degree of lithium coordination by PEO.

Attempts to extract chemical shift information for different samples were mostly inconclusive mainly because of the extremely wide signals (in the range of kilohertz). Yet at room temperature, a recognizable trend in chemical shift variation was observed in samples with varying degrees of reduction in the V_2O_5 layer. For example, the sample with the maximum load of Li^+, and hence with the most reduced V_2O_5 layer, shows the most up-field chemical shift of ca. −25 ppm (compared to the LiCl value of 0 ppm). Likewise, the sample with the least Li^+ content shows the most down-field chemical shift of ca −7.6 ppm, while the one with an intermediate content of Li^+ shows a chemical shift of −14 ppm. This trend may be due to paramagnetic contact or pseudocontact shifts exerted on the Li^+ nucleus, but contributions from different Li^+ coordination environments may not yet be ruled out.

Charge-Transport Properties. The conductivity of both the pristine and irradiated $(PEO)_xV_2O_5{\cdot}nH_2O$ samples decreases with increasing x. The pristine materials posses lower conductivities with a maximum at room temperature of $\sim 10^{-4}$ S/cm for $x = 0.5$. It has been reported that at high water content the conductivity of the $V_2O_5{\cdot}nH_2O$ xerogels is primarily protonic, particularly near room temperature.[23b] The irradiated $(PEO)_{0.5}V_2O_5{\cdot}nH_2O$ samples have nearly a 2 orders magnitude higher conductivity, up to 10^{-2} S/cm at room temperature, which drops to 5×10^{-4} S/cm in $(PEO)_{1.5}V_2O_5{\cdot}nH_2O$; see Table 5. This decrease is attributed to the increased spatial separation of the conductive V_2O_5 layers which increases the barrier for electron transport through the material. Variable-temperature electrical conductivity data are shown in Figure 13, and they are consistent, in all cases, with thermally activated small-polaron hopping.[33] Interestingly, the activation energy calculated from these data for both samples is similar at 0.24 eV. This may be a consequence of the fact that only minimal structural changes occur in the vanadium oxide framework upon PEO encapsulation. Similar charge-transport behavior was seen in other related intercalates of $V_2O_5{\cdot}nH_2O$.[6]

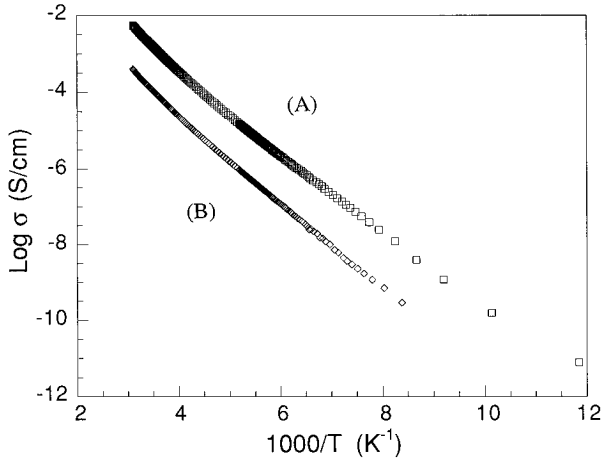

Figure 13. Variable-temperature electrical conductivity data for irradiated samples of (A) a $(PEO)_{0.5}V_2O_5{\cdot}nH_2O$ film and (B) a $(PEO)_{1.5}V_2O_5{\cdot}nH_2O$ film.

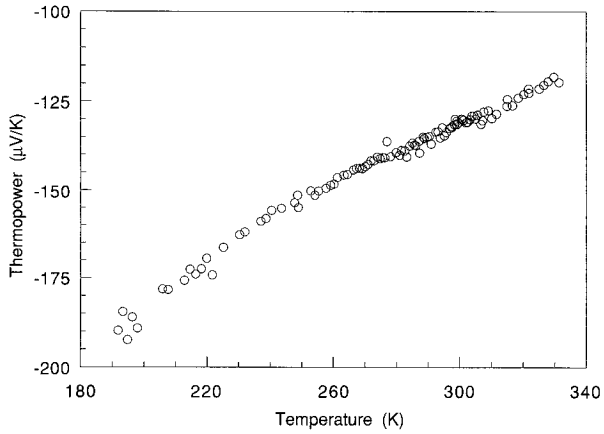

Figure 14. Thermoelectric power as a function of temperature for a $(PEO)_{0.5}V_2O_5{\cdot}nH_2O$ film.

Table 5. Room-Temperature Electrical Conductivity and Thermoelectric Power of Unirradiated and Irradiated $(PEO)_xV_2O_5{\cdot}nH_2O$ Materials

	conductivity σ (S/cm)		thermopower (μV/K)
x	unirradiated	irradiated	irradiated
0.5	10^{-4}	10^{-2}	−140
1.0	10^{-5}	10^{-3}	−150
1.5	10^{-6}	5×10^{-4}	−160

Thermoelectric power data could be measured reliably only for the irradiated materials because the pristine materials became too resistive at lower temperatures. The Seebeck coefficients are negative with large values and decrease with falling temperature, indicative of n-type thermally activated charge transport. Generally, the Seebeck coefficients are less negative (ca. −120 μV/K at room temperature for ir-$(PEO)_{0.5}V_2O_5{\cdot}nH_2O$) than those of the corresponding pristine materials (ca. −220

(30) (a) Wang, G.; Roos, J.; Brinkmann, D.; Pasquali, M.; Pistoia, G. *J. Phys. Chem. Solids* **1993**, *54*, 851−855. (b) Gang, W.; Roos, J.; Brinkmann, D.; Capuano, F.; Croce, F.; Scrosati, B. *Solid State Ionics* **1992,** *53*−*56*, 1102−1105. (c) Tanzella, F. L.; Bailey, W.;Frydrych, D.; Farrigton, G. C.; Story, H. S. *Solid State Ionics*, **1981**, *5*, 681−684. (d) Killis, A.; LeNest, J. F.; Gandini, A.; Cheradame, H.; Cohen-Addad, J. P. *Polym. Bull.* **1982**, *6*, 351−358. (e) Wintersgill, M. C.; Fontanella, J. J.; Calame, J. P.; Greenbaum, S. G.; Andeen, C. G. *J. Electrochem. Soc.* **1984**, *131*, 2208−2209.

(31) Greenbaum, S. G. *Solid State Ionics* **1985,** *15*, 259−262.

(32) Sondregger, M.; Roos, J.; Mali, M.; Brinkmann, D. *Solid State Ionics* **1992**, *5*, 849−852.

(33) (a) Bullot, J.; Cordier, P.; Gallais, O.; Gauthier, M.; Livage, J. *J. Non-Cryst. Solids* **1984**, *68*, 135−146. (b) Sanchez, C.; Henry, M.; Grenet, J. C.; Livage, J. *J. Phys. C: Solid State Phys.* **1982**, *15*, 7133−7141.

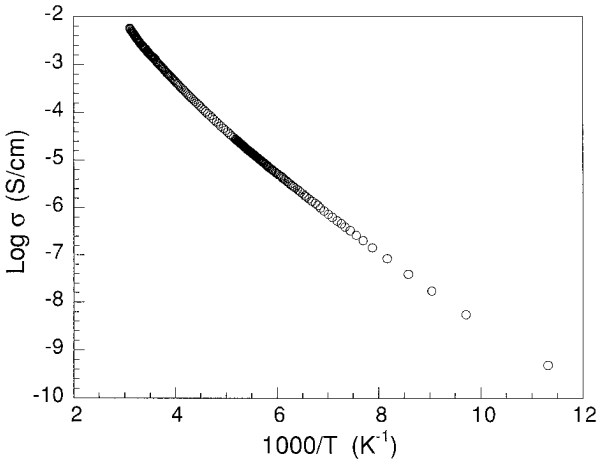

Figure 15. Variable-temperature electrical conductivity data for a sample of $Li_{0.18}(PEO)_{0.5}V_2O_5{\cdot}nH_2O$.

μV/K at room temperature); see Figure 14. The Seebeck coefficients increase toward more negative values with increasing amount of PEO (ca. -150 μV/K at room temperature for ir-$(PEO)_{1.5}V_2O_5{\cdot}nH_2O$), consistent with the order of decreasing conductivity and suggests a smaller number of carriers in the PEO-rich materials. The $Li_y(PEO)_xV_2O_5{\cdot}nH_2O$ materials generally show similar charge transport properties to those of the irradiated $(PEO)_xV_2O_5{\cdot}nH_2O$; see Figure 15. This is rationalized by the fact that these two sets of materials possess charge carriers (i.e., V^{4+} centers) of similar nature and quantity. This is evident from electron spin resonance and magnetic susceptibility measurements. Given the nature of this measurement (four-probe dc conductivity) we are observing only electronic conductivity.

Concluding Remarks

The use of water-swellable V_2O_5 xerogel as a host material has yielded a family of new PEO/V_2O_5 nanocomposite phases. The intercalation of PEO in $V_2O_5{\cdot}nH_2O$ produces new materials with interesting photochemical properties and lithium redox intercalation. The magnitude of increase in electrical conductivity upon irradiation depends on polymer loading. The enhanced electrical conductivity at room temperature is rationalized on the basis of increased carrier (spin) concentration in the vanadium oxide framework. Although ionic conduction is expected to contribute only a small fraction to the charge transport properties of the irradiated $(PEO)_{0.50}V_2O_5{\cdot}nH_2O$ films, it probably plays a more significant role in the pristine films. We expect that by adjusting this loading we can obtain inclusion compounds with controlled light sensitivity and electrical conductivity. LiI can serve to prepare several $Li_y(PEO)_xV_2O_5{\cdot}nH_2O$ phases. NMR spectroscopy shows that Li is mobile and could impart good ionic conductvity to the composite materials. The data however do not conclusively prove that the Li^+ ions are coordinated by PEO.

Acknowledgment. Financial Support from the National Science Foundation (DMR-93-06385) is gratefully acknowledged. This work made use of the SEM facilities of the Center for Electron Optics at Michigan State University. At Northwestern University this work made use of Central Facilities supported by the NSF through the Materials Research Center (DMR-91-20521).

CM950366O